Materials Technology Reports 2025, 3(1), 2851.
https://doi.org/10.59400/mtr2851

Article

Sinterability, structural evolution and pinhole elimination of high strength self-glazed glass-ceramics sintered from granite sludge by instant glaze firing

Changyou Liu, Jian Zhou, Jinshan Lu*

School of Power and Energy, Nanchang Hangkong University, Nanchang 330063, China
*** Corresponding author:** Jinshan Lu, 1474202488@qq.com

CITATION

Liu C, Zhou J, Lu J. Sinterability, structural evolution and pinhole elimination of high strength self-glazed glass-ceramics sintered from granite sludge by instant glaze firing. Materials Technology Reports. 2025; 3(1): 2851. https://doi.org/10.59400/mtr2851

ARTICLE INFO

Received: 26 February 2025
Accepted: 1 April 2025
Available online: 7 April 2025

Abstract: Granite sludge from the cutting and polishing of granite blocks should be utilized to prevent environmental pollution. This study focuses on the preparation of high-strength self-glazed glass-ceramics from granite sludge by combining dense sintering and instant glaze firing. Thermal analyses including thermogravimetry, differential scanning calorimetry and thermal expansion were used to evaluate the sinterability of the granite powder and to determine the dense sintering temperature. For the instant glaze firing of the sintered glass-ceramics, the structural evolution was analyzed by *X*-ray diffraction and solid-state nuclear resonance to clarify glaze formation and glass network stability, respectively. Glaze formation resulted from the dissolution of quartz and feldspars and the reduced glass viscosity, as indicated by the thermochemical calculation. As the glaze firing temperature was increased, the thickness of the surface glaze increased. The coefficient of thermal expansion of the glazed glass-ceramics indicates a residual compressive stress in the surface glaze. The elimination of glaze pinholes was achieved by reducing the amount of ferrous minerals and increasing the glaze firing rate. Under the optimum conditions, the flexural strength and surface glossiness of the glazed glass-ceramic were 112.5 MPa and 54.7 GU respectively, enabling the scalable production of high-strength self-glazed glass-ceramics from granite sludge for application in decorative tiles.

Keywords: granite sludge; instant glaze firing; glazed glass-ceramic; glaze formation; oversintering; glaze pinhole

1. Introduction

The cutting and polishing of granite blocks generates large quantities of granite sludge, which accounts for approximately 30% of granite blocks. Improper disposal poses potential hazards to soil, water and air [1]. The utilization of granite sludge is not only an efficient recycling of solid waste, but also beneficial to the environment. With the main minerals being quartz and feldspars, granite sludge has been used in various fields, including concrete, geopolymers, fluxes and composites [2–6]. However, disadvantages such as low utilization rates, high disposal costs and low added value have seriously hindered commercial practices [7].

As for the utilization in glass-ceramics, the R_2O-CaO-MgO-Al_2O_3-SiO_2 glass-ceramics were prepared from granite tailings by melting and bulk crystallization. The crystallization and preferential precipitation of hornblende resulted in superior flexural strength and excellent chemical resistance [8]. Similarly, high-strength mica-diopside-based glass-ceramics have been produced from granite waste using CaF_2 as a nucleating agent and fluxing agent. Increasing the SiO_2/Al_2O_3 ratio facilitated the

precipitation of diopside, kalsilite and tainiolite phases in the glass-ceramics, which exhibited superior fracture toughness of 3.28 $MPa \cdot m^{1/2}$ [9]. Architectural glass-ceramics were prepared from granite powder and marble waste by melt quenching and powder sintering. The main crystal phase varied with the marble content [10]. Copper red glass-ceramics were prepared from granite waste, CuO and other additives. The red glass-ceramic with 5 mass% CuO had superior mechanical properties [11]. In another way, anorthite glass-ceramics were rapidly sintered from the modified granite powder with the addition of boehmite, showing the strengthening and toughening of sintered glass-ceramics [12].

Porous ceramics have various applications in thermal and acoustic insulation, catalyst support, filtration and wastewater treatment [13,14]. Granite scraps were sintered with 14 mass% clay tailings and 1 mass% SiC at 1250 ℃ to produce a foamed ceramic with a porosity of 83.3% and a thermal conductivity of 0.051 $W \cdot m^{-1} \cdot K^{-1}$ [15]. Using a mixed foaming agent of SiC and MnO_2, foamed glass-ceramics were produced from granite tailings by melt quenching and powder sintering. The foaming process occurred near the phase transition point (880 ℃, quartz → tridymite) [16].

In the case of industrial practice, the production of architectural glass-ceramics from granite waste is a technically feasible and value-added route. However, the bulk crystallization process is characterized by high energy consumption and carbon emissions compared to the sintering process [17,18]. In addition, the black appearance of architectural glass-ceramics caused by the ferrous minerals drastically reduces their commercial value, but the decorative nature has hardly been considered so far [19]. In this paper, granite sludge was recycled into decorative architectural glass-ceramics by combining dense sintering and instant glaze firing. Sintering densification and glaze formation were clarified by thermal analysis and structural evolution in the glazed glass-ceramics, respectively. The glass network structure and stress distribution in the surface glaze were also investigated. Finally, glaze pinholes were removed to improve the decorativeness of the glazed glass-ceramics.

2. Materials and methods

2.1. Materials

Granite sludge was supplied by a stone processing plant in Fujian Province. After rinsing with distilled water to remove soluble impurities, the granite powder (GP) was passed through an 80-mesh sieve. As grinding media, ZrO_2 beads (NanorZr-95, ∅1–4 mm) were purchased from Guangzhou Pleased Grinding Media Co. Ltd. An NdFeB magnetic rod (∅25 mm × 200 mm, 1.2 T) was purchased from Jiangsu Hongsheng Magnetic Co. Ltd for magnetic separation. Analytical grade hydrochloric acid was used for acid leaching. Polyvinyl alcohol (PVA 1788, purity 87.4%) was purchased from Guangzhou Suixin Chemical Co. Ltd.

2.2. Preparation of glazed glass-ceramics

With a bead/powder mass ratio of 3:1 and a solids content of 20%, the GP powder was ground in an aqueous suspension with ZrO_2 beads in a planetary ball mill (XQM, Changsha Tianchuang) at 380 rpm for 1 h. The ground slurry was diluted and magnetic

separation was carried out using an NdFeB magnetic rod to remove the ferromagnetic ferrous minerals. The milled powder (MP) was passed through a 120-mesh sieve. To further reduce the colored ferrous minerals, the MP powder was acid leached by grinding in a 5 wt% HCl solution for 1 h, and the pickling powder (PP) was used as a feedstock to remove the glaze pinholes.

After granulation of the MP powder with an aqueous PVA solution, rectangular bars were compacted at 130 MPa using a stainless-steel mold (45 mm × 5 mm) and square plates were compacted at 30 MPa using a square mold (40 mm × 40 mm). To prepare the glazed glass-ceramics, the powder compacts were first densely sintered in a muffle furnace (KSX2-4-13, Xiangtan Xiangyi) at 1100 °C for 2 h and then the temperature was raised to 1150–1300 ℃ at a heating rate of 10 K·min^{-1} for the instant glaze firing without holding time (t = 0). The stepwise sintering process of these powder compacts is schematically shown in **Figure 1**.

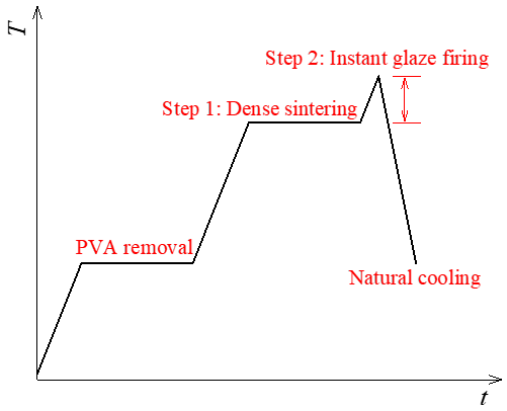

Figure 1. Schematic representation of the stepwise sintering process of powder compacts.

2.3. Characterization and measurements

The crystal structure of the powders and glass-ceramics was examined by *X*-ray powder diffraction (XRD，D8 Advance，Bruker AXS) using Cu K_α radiation, and the degree of crystallization and phase composition (vol%) were calculated using the supplied TOPAS 4.2 software. The chemical composition of the powders was analyzed by *X*-ray fluorescence spectroscopy (XRF, S4 PIONEER, Bruker AXS). The particle size distribution of the powders was determined using a laser scattering particle size analyzer (BT-9300ST, Bettersize).

The thermal behavior of different powders was analyzed by thermogravimetry and differential scanning calorimetry (TG-DSC, STA 8000, PE). The measurements were carried out in an air atmosphere at a heating rate of 20 K·min^{-1}. To analyze the sintering kinetics of the powder compacts and to evaluate the stress distribution in the surface glaze, the linear expansion of rectangular bars (10 mm × 6 mm × 5 mm) was monitored using a thermal dilatometer (TMA 402F3, Netzsch) measured at a heating rate of 10 K·min^{-1} and a nitrogen flow rate of 50 mL·min^{-1}. The glass network structure of the glazed glass-ceramics was analyzed using the ^{29}Si spectra measured by a magic angle spinning nuclear magnetic resonance spectrometer (MAS-NMR, Avance Neo 400WB, Bruker) with a H/X dual resonance solid-state probe. The ^{29}Si chemical shifts

are reported in δ(ppm) relative to the reference tetramethyl silane. The glaze pinholes were observed using a 3D ultra-depth field optical microscope (VHX-600E, Keyence). The microstructure of the powders and glass-ceramics was observed by scanning electron microscopy (SEM, Sigma 300, Zeiss) with an attached *X*-ray energy dispersive spectrometer (EDS, Smart EDX, Zeiss) to identify the mineral phases. A platinum film was deposited on the samples to increase the surface conductivity.

Powder whiteness was measured with a portable whiteness meter (WSB-1, Qiwei) using blue light reflectance (R457). The bulk density of the glass-ceramics was measured using the Archimedes method. The surface glossiness of the square glazed glass-ceramics was measured using a portable glossiness meter (WGG 60, Hunan Lichen), the value being an average of five tests. The flexural strength of the glass-ceramics was measured using rectangular bars (35 mm × 4 mm × 3 mm) in an Instron-type apparatus (WDW-50, Jinan Shijin) at a crosshead speed of 1 mm·min^{-1}. Flexural strength is an average value of three individual tests.

3. Results and discussion

3.1. Characterization of different powders

Figure 2 shows the XRD patterns of different powders. The mineral composition of the GP powder includes quartz (SiO_2, PDF#46-1045), albite ($(Na,Ca)Al(Si,Al)_3O_8$, PDF#41-1480), anorthite ($(Ca,Na)(Al,Si)_2Si_2O_8$, PDF#20-0528) and microcline ($KAlSi_3O_8$, PDF#19-0932) with relative contents of 49.7%, 15.8%, 33.0% and 1.5%, respectively. In addition, a trace phase of cummingtonite ($(Fe_{0.6}Mg_{0.4})_7Si_8O_{22}(OH)_2$, PDF#42-0545) is associated with the microcline mineral [20]. After ball milling and magnetic separation, the cummingtonite phase disappeared and the diffraction intensities of the feldspar minerals in the MP powder are significantly reduced due to particle size refinement and partial amorphization [21].

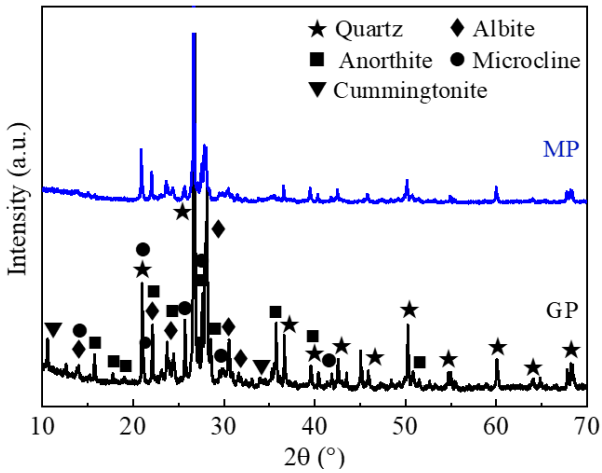

Figure 2. XRD patterns of GP and MP powders.

Table 1 shows the XRF results of different powders. The main components include SiO_2, Al_2O_3, CaO, Na_2O and K_2O, which are closely related to quartz and feldspars. Due to high Fe_2O_3 content in the GP powder, the reduction reaction of Fe_2O_3 occurred spontaneously during the sintering process, leading to self-foaming of the

sintered ceramics [22]. After magnetic separation, the Fe_2O_3 content in the MP powder decreased significantly from 4.39% to 0.63% and the TiO_2 content decreased from 0.87 % to 0.15%. XRD analysis showed that the ferromagnetic impurities from the magnetic separation included magnetite (Fe_3O_4, PDF#89-2355) and quartz. The entrainment of the quartz phase may be related to the associated minerals. Magnetic separation not only removed magnetite and cummingtonite, but also reduced traces of ilmenite [23]. The pickling treatment further reduced the Fe_2O_3 content to 0.37% in the PP powder. As most of the colored iron-bearing minerals have been removed, the powder whiteness increases greatly from 48.6% (GP) to 82.1% (MP) and 87.3% (PP).

Table 1. Chemical composition of different powders (mass%).

Powders	SiO_2	Al_2O_3	CaO	Fe_2O_3	K_2O	Na_2O	MgO	TiO_2	P_2O_5	MnO	Else
GP	64.97	14.81	5.87	4.39	4.10	3.15	1.29	0.87	0.20	0.09	0.26
MP	69.53	15.78	6.22	0.63	3.60	3.37	0.21	0.15	0.18	-	0.33
PP	72.55	15.25	4.41	0.37	3.48	2.82	0.06	0.16	0.07	-	0.83

Figure 3 shows the SEM images of different powders. The particles are mostly layered, which is characteristic of aluminosilicate minerals. EDS analysis shows that the MP powder consists of microcline (particle 1), quartz (particle 2), anorthite (particle 3) and albite (particle 4) phases. **Figure 4** shows the particle size distribution of different powders. Compared to the GP powder, the MP powder shows a more uniform and narrower size distribution. The median particle size (D_{50}) is significantly reduced from 19.7 μm (GP) to 3.6 μm (MP) due to particle pulverization during the milling process, which is consistent with the SEM observation.

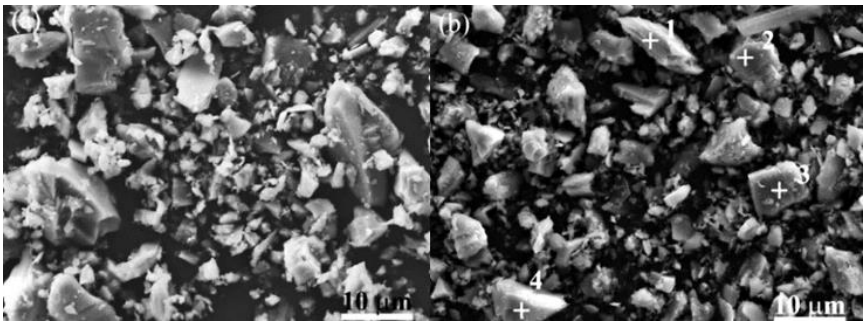

Figure 3. SEM images of different powders: **(a)** GP; **(b)** MP.

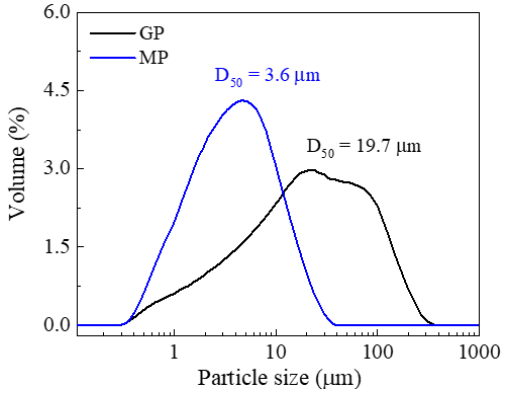

Figure 4. Particle size distribution of GP and MP powders.

3.2. Thermal analysis of powders and powder compacts

Figure 5 shows the thermal analyses of both powders and powder compacts. From the TG-DSC curves, there were weak endothermic peaks at 660–673 ℃ accompanied by weight losses of 0.8%–1.2%. This is related to the thermal decomposition of the associated calcite minerals in the granite and the Al-carbonate complexes formed during the carbonation of the anorthite phase [24,25]. As the temperature was increased to around 1000 ℃, there was strong endothermic behavior due to the initial melting of the albite phase (T_m = 1100 ℃). Compared to the GP powder, the MP powder showed slightly lower decomposition and melting temperatures, which can be attributed to the small size effect of powders [26,27].

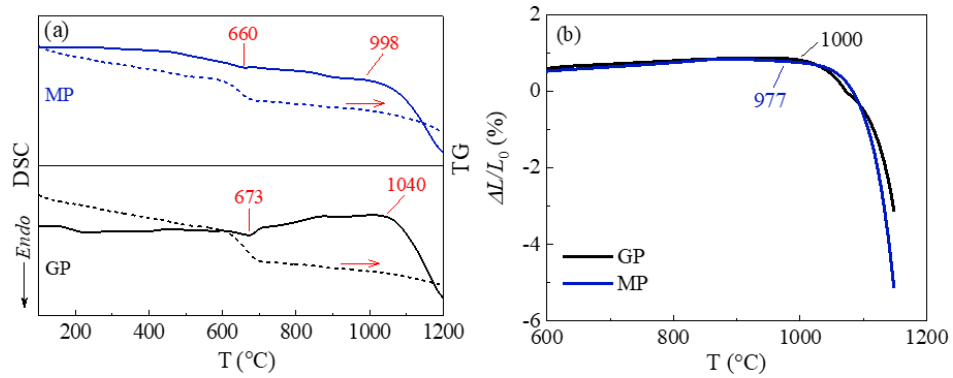

Figure 5. (a) TG-DSC curves of the powders; **(b)** linear thermal expansion curves of the powder compacts.

In **Figure 5b**, the initial sintering temperature for the MP compact is 977 ℃, which is slightly lower than the 1000 ℃ for the GP compact. The densification rate of the powder compacts at the rapid shrinkage stage was calculated to be 103 μm·min^{-1} (GP) and 171 μm·min^{-1} (MP). The smaller the particle size, the lower the initial sintering temperature and the higher the densification rate [28]. The refinement of particle size increases the sintering activity of powders and improves the densification of powder compacts. Considering the powder whitening that occurred after magnetic separation, the MP powder was used as the raw material in the following experiments. The dense sintering temperature of the MP compact was determined to be 1100 ℃, which was confirmed in the sintering experiments [29].

3.3. Structural evolution in instant glaze firing

In the case of the glazed glass-ceramics, the powder compact was subjected to a dense sintering process at 1100 ℃, followed by an instant glaze firing at 1300 ℃. **Figure 6** shows the crystal structure of the surface glaze and the interior of the glazed glass-ceramic. The surface glaze is dominated by the glass phase, with a crystallinity of 9.0%. In contrast, the interior shows a higher degree of crystallinity at 46.2%, with quartz (25.5%) and anorthite (14.8%) phases that are much higher than those observed in the surface glaze (**Figure 6b**). This discrepancy in crystal composition suggests that glaze formation is closely related to the increased glass phase due to the dissolution of quartz and feldspars in the liquid glass phase [30].

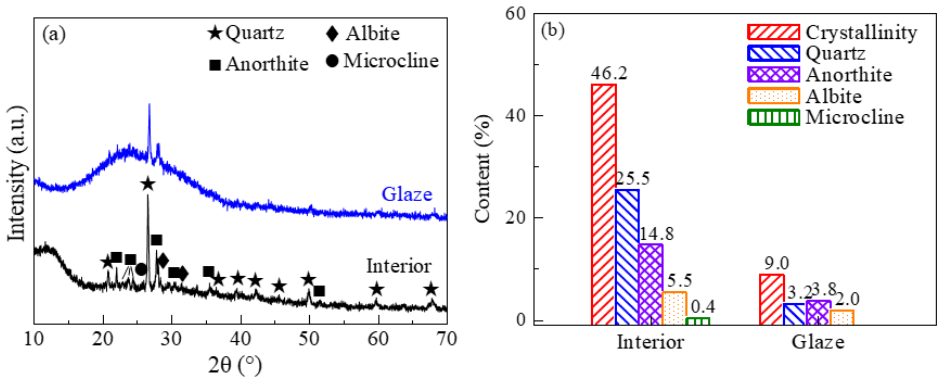

Figure 6. Crystal structure of the glazed glass-ceramic: **(a)** XRD pattern; **(b)** phase content.

In the silicate glasses, the type of Q^n structural units was determined by the chemical shift in the MAS-NMR spectra, and the content of Q^n structural units was quantitatively analyzed by the Gaussian peak area ratio [31]. **Figure 7** shows the ^{29}Si MAS-NMR spectra of the glazed glass-ceramics at different firing temperatures. The ^{29}Si resonance peaks were deconvoluted into two symmetrical peaks centered at −93.8 ppm and −103.4 ppm, which were assigned to the Q^3 and Q^4 structural units in the glass network of SiO_4 tetrahedra, respectively [32]. When the glaze firing temperature was increased from 1150 °C to 1300 °C, the Q^3/Q^4 ratio decreased significantly from 0.81 to 0.66. This indicates that the dissolution of the anorthite phase in the glass phase reduced the amount of non-bridging oxygen, which strengthened the SiO_4 networks by the connection of AlO_4 tetrahedra [33].

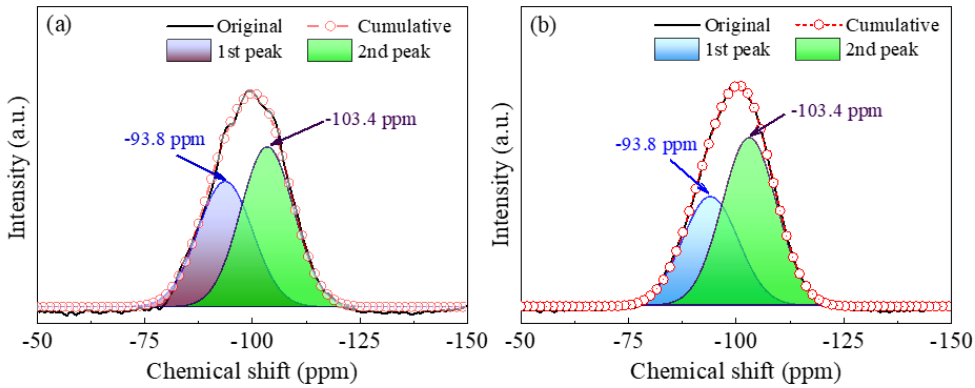

Figure 7. ^{29}Si MAS-NMR spectra of the glazed glass-ceramics at different glaze firing temperatures: **(a)** 1150 °C; **(b)** 1300 °C.

Figure 8 shows the digital photographs of the powder compact at different stages of sintering. After dense sintering of the powder compact, most of the original pores have been removed, resulting in significant shrinkage of the sintered glass-ceramic. However, black patches of colored minerals from the MP powder remain in the sintered glass-ceramic, indicating a small amount of dissolution in the liquid glass phase. The instant glaze firing created a temperature gradient between the surface and the interior. The surface was exposed to the high-temperature environment, which reduced the glass viscosity and accelerated the dissolution of quartz and feldspars, thereby promoting glaze formation [34]. Instant glaze firing mitigated thermal damage

to the internal structure, resulting in a high-strength glazed glass-ceramic. In particular, black spots disappeared after instant glaze firing as the colored minerals dissolved into the liquid glass phase.

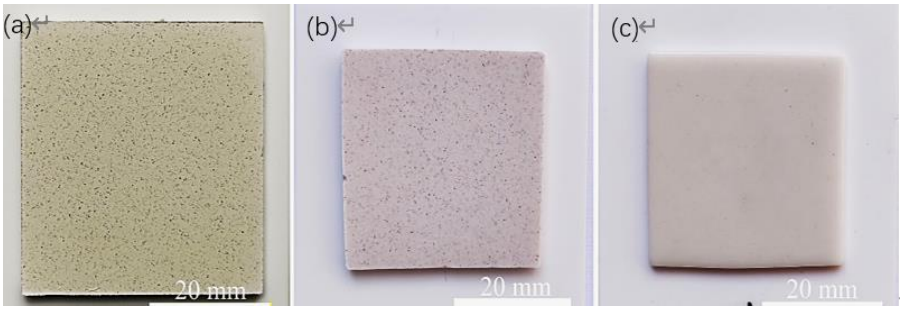

Figure 8. Digital photographs of samples at different stages of sintering: **(a)** Powder compact; **(b)** densely sintered glass-ceramic; **(c)** glazed glass-ceramic.

3.4. Physical properties of glazed glass-ceramics

Figure 9a shows the bulk density and flexural strength of the glazed glass-ceramics. The bulk density and flexural strength generally decreased with increasing firing temperature, especially above 1250 ℃. Besides oversintering of the glass-ceramics, self-foaming caused by the iron-bearing minerals is mainly responsible for the decrease in bulk density above 1200 ℃ [35]. As the firing temperature increased from 1250 ℃ to 1300 ℃, the flexural strength decreased dramatically from 106.9 MPa to 79.7 MPa. In contrast, the surface glossiness increased continuously with increasing firing temperature (**Figure 9b**), reaching 61.6% at 1300 ℃. This is attributed to the reduced viscosity and improved leveling of the liquid glass phase, as evidenced by the passivated sample edges above 1250 ℃ in the inset image. In addition, the dissolution of colored iron-bearing minerals in the liquid glass phase reduced the light absorption and increased the surface glossiness [36].

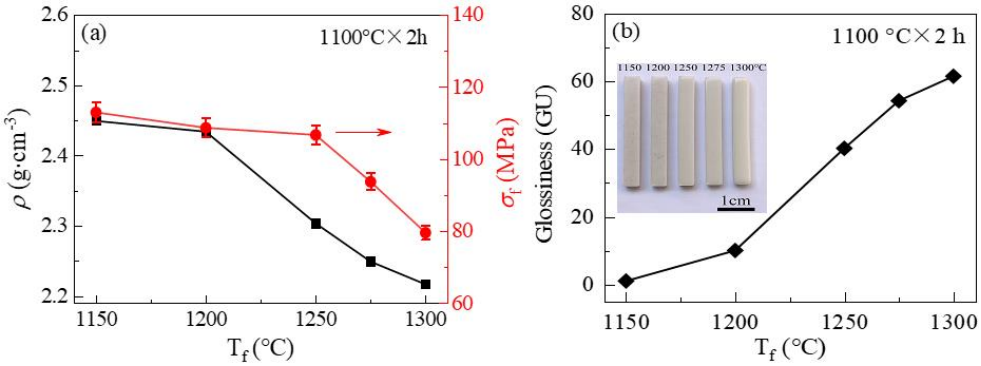

Figure 9. Physical properties of the glazed glass-ceramics at different firing temperatures: **(a)** Bulk density and flexural strength; **(b)** surface glossiness.

In the instant glaze firing, the viscosity variation of the glass melt was studied by thermochemical calculation using the viscosity module and melt database of FactSage 8.1 software (GTT-Technologies and Thermfact/CRCT, Germany/Canada) based on the chemical composition of the MP powder [37,38]. In **Figure 10**, it is clear that the glass viscosity decreases dramatically with increasing firing temperature, especially

below 1250 °C. This follows an exponential decrease in glass viscosity. From the linear simulation of $\ln\eta$ against 1000/T, the activation energy (E_η) for the viscous flow of the glass phase was calculated from the slope (E_η/R, where R is the ideal gas constant), resulting in a value of 379 kJ·mol^{-1}.

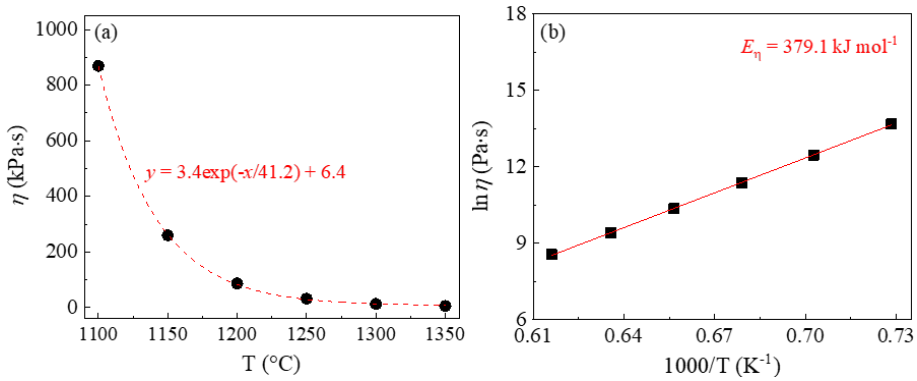

Figure 10. Variation of the glass melt viscosity with firing temperature: **(a)** Viscosity; **(b)** linear simulation.

Figure 11 shows the cross-sectional SEM images of the glazed glass-ceramics. At the firing temperature of 1250 °C, the glaze layer had a thickness of 30–45 μm, which increased drastically to 100–115 μm at 1300 °C. Furthermore, a few large pores in the interior are related to oversintering, and glaze pinholes (yellow arrows) degrade the decorativeness of glazed glass-ceramics. In **Figure 11c**,**d**, the composition contrast shows that increasing the glaze firing temperature significantly reduced the crystallinity (white crystallites) of the glazed glass-ceramics, implying the gradual dissolution of quartz and anorthite into the liquid glass phase. The increasing glass phase with reduced viscosity favors the leveling of the liquid glass, which explains the increased surface glossiness of the glazed glass-ceramics at elevated temperatures.

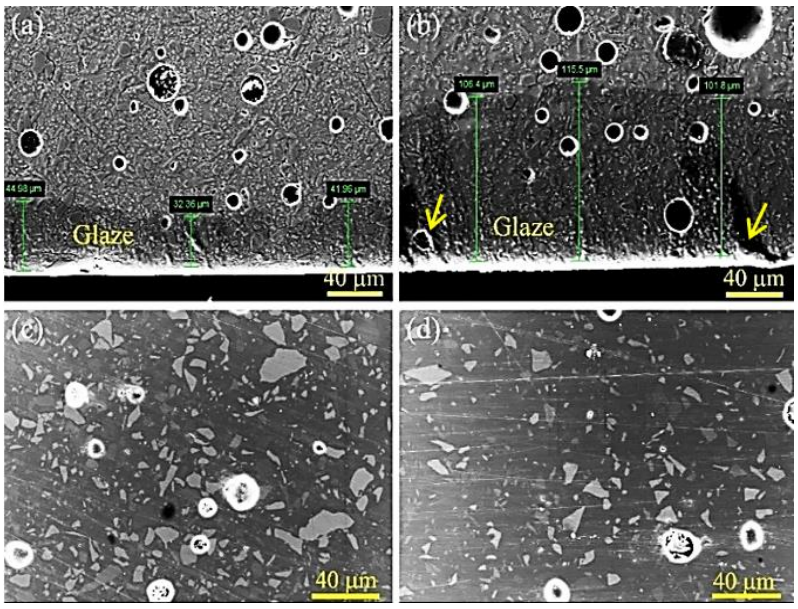

Figure 11. SEM images of the glazed glass-ceramics at different firing temperatures. **(a)** the cross-section at 1250 °C; **(b)** the cross-section at 1300 °C; **(c)** the interior at 1250 °C; **(d)** the interior at 1300 °C.

Figure 12 shows the thermal expansion curves of the glass-ceramics with and without (polished) the surface glaze. Below 600 °C, the coefficient of thermal expansion of the glazed glass-ceramic is slightly lower than that of the glass-ceramic without the glaze layer, indicating that the glaze layer limited the expansion of the interior as the temperature increased. In other words, the residual compressive stress was generated in the glaze layer when the glazed glass-ceramic was cooled down to room temperature. The similar coefficient of thermal expansion and the compressive stress in the surface glaze are beneficial for the thermal shock resistance of the glazed glass-ceramics [39].

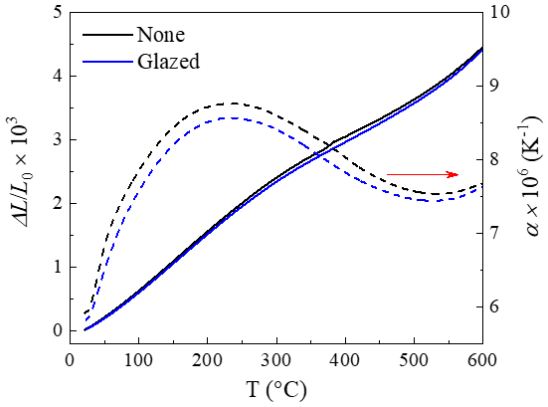

Figure 12. Thermal expansion curves (solid lines) and coefficient of thermal expansion curves (dashed lines) of the glass-ceramics with (blue) and without (black) the surface glaze.

3.5. Formation and elimination of glaze pinholes

Pinholing, defined as a sub-millimeter pit on the glaze surface, is one of the most significant glaze defects in building tiles and porcelain. It is therefore of paramount importance to strictly control this phenomenon in commercial production [40]. Pinholing is ascribed to the migration of small gas bubbles from the interior of the glaze layer to the surface, resulting in the formation of small craters after cooling. Pinhole defects can be minimized by optimizing the composition and sintering profile of the glaze, which in turn increases the proportion of qualified products [41,42]. Herein, the formation of pinholes was studied in relation to the glaze firing process and chemical composition, and countermeasures were taken to eliminate the defects.

In the instant glaze firing, oversintering promoted the release of residual pores and the formation of pinholes. The increase in liquid glass with reduced viscosity led to an increase in the number of glaze pinholes at high firing temperatures. **Figure 13** presents digital photographs and optical images of the glazed glass-ceramics at 1300 °C. The glazed glass-ceramic with a light-yellow color has a surface glossiness of 61.6 GU, but shows a high prevalence of glaze pinholes (50–200 μm) (**Figure 13a**). Increasing the heating rate of the glaze firing from 10 K·min^{-1} to 50 K·min^{-1} resulted in a significant reduction in the surface exposure to the high temperature environment. The glaze color changed from light yellow to cyan, and the pinhole density was significantly reduced (**Figure 13b**), with a surface glossiness of 53.4 GU. The discrepancy in glaze color and surface glossiness is due to the reduced glass phase and

reduced dissolution of colored minerals. Color mapping of the glaze surface demonstrates an improvement in surface roughness and a reduction in pinholes at the accelerated glaze firing rate.

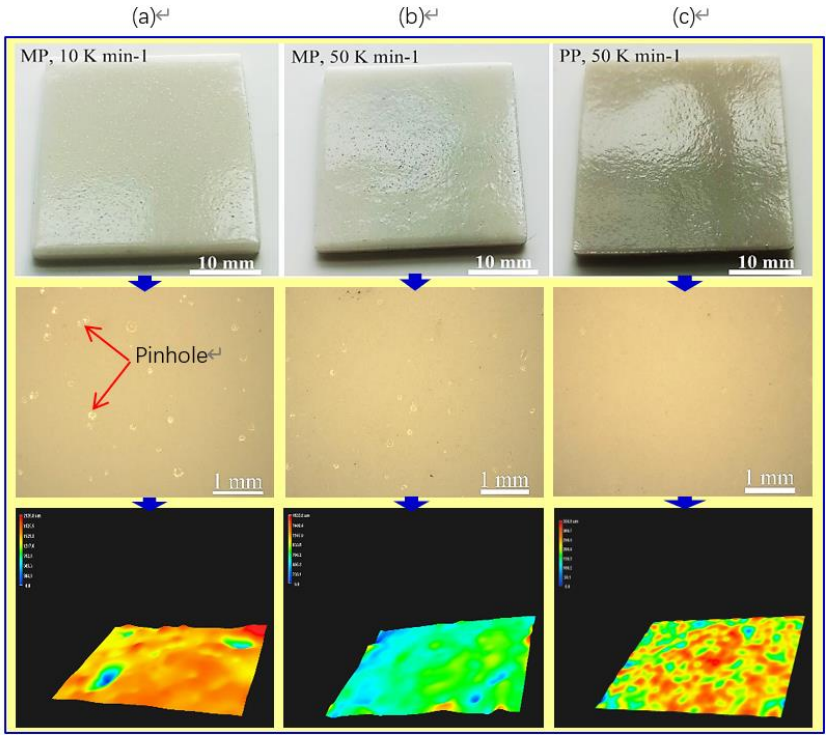

Figure 13. Digital photographs (top) and optical images (middle and bottom) of the glazed glass-ceramics sintered from different powders. **(a)** MP; **(b)** MP; **(c)** PP.

In addition to the aforementioned oversintering process, the reduction reaction of ferric iron to ferrous iron during the glaze firing released oxygen gas, resulting in self-foaming of the glazed glass-ceramics [43]. As listed in **Table 1**, the concentration of ferric oxide in the PP powder was reduced to 0.37%. As a result, the glaze surface is free of pinholes (**Figure 13c**). The surface glossiness is 54.7 GU, which is slightly higher than that observed in the MP powder (**Figure 12b**). Moreover, the sinterability of the glaze could be improved by increasing the glaze firing rate and reducing the average particle size [44]. Consequently, the elimination of pinholes was achieved by increasing the glaze firing rate and reducing the amount of colored iron-bearing minerals.

Figure 14 shows the crystal structure of the glazed glass-ceramics at a firing temperature of 1300 °C. The glass-ceramic produced from the PP powder exhibits a slightly higher degree of crystallinity than that produced from the MP powder (52.3% vs. 46.2%). As shown in **Table 1**, the pickling treatment resulted in a slight reduction in the Na_2O and K_2O contents due to the acid leaching of albite and microcline [45]. This resulted in a reduction of the liquid glass phase during glaze firing and an increase in the crystallinity of the glazed glass-ceramics. The D_{50} value decreased from 3.60 μm (MP) to 1.92 μm (PP). The bulk densities of the glazed glass-ceramics were 2.22 $g \cdot cm^{-3}$ (MP) and 2.33 $g \cdot cm^{-3}$ (PP), while the flexural strength increased significantly from 79.7 MPa (MP) to 112.5 MPa (PP). The increased densification and crystallinity contribute to the strengthening of the glazed glass-ceramics.

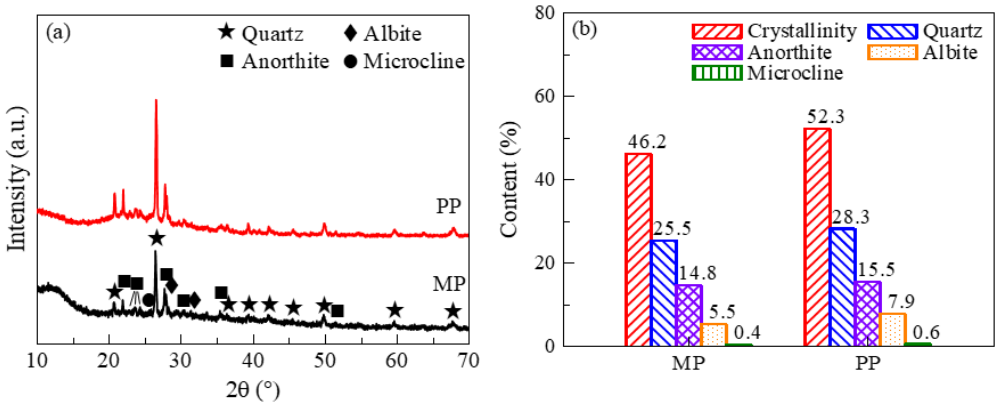

Figure 14. Crystal structure of the glazed glass-ceramics produced from MP and PP powders: **(a)** XRD pattern; **(b)** phase content.

When the firing temperature was increased to 1325 ℃, the glaze color changed to a milky white with a surface glossiness of 67.6 GU (**Figure 15a**). Increasing the firing temperature improves the leveling of the liquid glass phase, resulting in an increase in surface glossiness. Similarly, the glazed glass-ceramics with different colors were prepared with the addition of 0.5% by mass of colorants (**Figure 15b–d**). The smooth and bright glazes show an aesthetic appearance, indicating that the glazed glass-ceramics are suitable for applications in decorative building tiles and high-temperature glazes.

Figure 15. Digital photographs of the glazed glass-ceramics doped with different colorants.

4. Conclusions

High-strength glazed glass-ceramics have been produced entirely from granite sludge by dense sintering and instant glaze firing. Thermal analyses show that the MP powder could be densely sintered by liquid phase sintering at 1100 °C. In the instant glaze firing, a temperature gradient was created to mitigate thermal damage to the interior of the glazed glass-ceramics. Glaze formation was associated with an increase in the liquid glass phase due to the dissolution of quartz and feldspars, which improved

the stability of the SiO_4 networks. Thermal expansion analysis indicated the presence of residual compressive stress in the surface glaze. Finally, glaze pinholes could be eliminated by increasing the glaze firing rate and reducing the amount of colored iron-bearing minerals. A pinhole-free glazed glass ceramic with a flexural strength of 112.5 MPa and a surface gloss of 54.7 GU was produced from the PP powder. Various colored glazed glass-ceramics were prepared by the addition of suitable colorants, thus promising the industrial production of decorative building tiles from granite sludge.

Author contributions: Conceptualization, CL and JL; methodology, CL and JL; software, JZ; validation, CL and JZ; formal analysis, CL and JL; investigation, CL and JZ; resources, JL; data curation, CL; writing—original draft preparation, CL; writing—review and editing, JL; visualization, JL; supervision, JL; project administration, JL; funding acquisition, JL. All authors have read and agreed to the published version of the manuscript.

Funding: This work was financially supported by the National Natural Science Foundation of China (Grant No. 52060020).

Conflict of interest: The authors declare no conflict of interest.

References

1. Careddu N, Siotto G, Siotto R, et al. From landfill to water, land and life: The creation of the Centre for stone materials aimed at secondary processing. Resources Policy. 2013; 38(3): 258-265. doi: 10.1016/j.resourpol.2013.05.001
2. Hou W, Zhang Q, Zhuang ZB, et al. Sustainable reusing marble powder and granite powder in cement-based materials: a review. ACS Sustainable Chemistry & Engineering. 2024; 12(7): 2484-2510. doi: 10.1021/acssuschemeng.3c06670
3. Luo YP, Bao SX, Liu S, et al. Enhancing reactivity of granite waste powder toward geopolymer preparation by mechanical activation. Construction and Building Materials. 2024; 414: 134981. doi: 10.1016/j.conbuildmat.2024.134981
4. Ngayakamo B, Bello A, Onwualu AP. Valorization of granite waste powder as a secondary flux material for sustainable production of ceramic tiles. Cleaner Materials; 2022. doi: 10.1016/j.clema.2022.100055
5. Sripriyan K, Karthigha M. Influence of granite micro particles on the mechanical, damping and antimicrobial properties of silk-sisal hybrid composites. Scientific Reports. 2024; 14: 15995. doi: 10.1038/s41598-024-63190-w
6. Sripriyan K, Aravind S, Gopinath S, et al. Effect of granite filler on the mechanical and damping behaviour of silk-sisal hybrid composite for automobile applications. International Journal of Product Sound Quality. 2023; 1(1): 18-28. doi: 10.1504/IJPSQ.2023.133660
7. Surra E, Sousa J, Correia M, et al. Technical, environmental, and cost assessment of granite sludge valorisation. Applied Sciences. 2023; 13(7): 4513. doi: 10.3390/app13074513
8. Luo Y, Wang F, Liao Q, et al. Effect of TiO_2 on crystallization kinetics, microstructure and properties of building glass-ceramics based on granite tailings. Journal of Non-Crystalline Solids. 2021; 572: 121092. doi: 10.1016/j.jnoncrysol.2021.121092
9. Tian X, Li A, Li S, et al. Crystallization behavior and mechanical properties of high strength mica-containing glass-ceramics from granite wastes. Ceramics International. 2022; 48(16): 23119-23126. doi: 10.1016/j.ceramint.2022.04.292
10. Luo Y, Bao S, Zhang Y. Recycling of granite powder and waste marble produced from stone processing for the preparation of architectural glass–ceramic. Construction and Building Materials. 2022; 346: 128408. doi: 10.1016/j.conbuildmat.2022.128408
11. Xue J, Zhong J, Mao Y, et al. Effect of CuO on crystallisation and properties of red R_2O–CaO–MgO–Al_2O_3–SiO_2 glass-ceramics from granite wastes. Ceramics International. 2020; 46(14): 23186-23193. doi: 10.1016/j.ceramint.2020.06.099
12. Lu J, Li Y, Zou C, et al. Effect of heating rate on the sinterability, crystallization, and mechanical properties of sintered glass–ceramics from granite waste. Journal of Thermal Analysis and Calorimetry. 2018; 135(4): 1977-1985. doi: 10.1007/s10973-018-7346-0

13. Vakifahmetoglu C, Semerci T, Soraru GD. Closed porosity ceramics and glasses. Journal of the American Ceramic Society. 2020; 103(5): 2941-2969. doi: 10.1111/jace.16934
14. Zhang J, Liu B, Zhang S. A review of glass ceramic foams prepared from solid wastes: processing, heavy-metal solidification and volatilization, applications. Science of The Total Environment. 2021; 781: 146727. doi: 10.1016/j.scitotenv.2021.146727
15. Jiang C, Huang S, Li G, et al. Formation of closed-pore foam ceramic from granite scraps. Ceramics International. 2018; 44(3): 3469-3471. doi: 10.1016/j.ceramint.2017.10.180
16. Deng F, Wang F, Shi X, et al. Synthesis and properties of foam glass-ceramics from granite tailings by using SiC and MnO_2 as the mixed foaming agent. Ceramics International. 2023; 49(22): 34647-34656. doi: 10.1016/j.ceramint.2023.08.120
17. Liu XM, Li B, Wu YF, The pretreatment of non-ferrous metallurgical waste slag and its research progress in the preparation of glass-ceramics. Journal of Cleaner Production. 2023; 404: 136930. doi: 10.1016/j.jclepro.2023.136930
18. Wilkinson C. Glass and a carbon-free United States: What is glass's role in the upcoming green revolution? Journal of the American Ceramic Society. 2024; 107(3): 1533-1542. doi: doi.org/10.1111/jace.19360
19. Wang W, Wang K, Zhang J, et al. Effect of process parameters on characteristics and pore structure of foam ceramics prepared from granite sawing dust. Ceramics International. 2024; 50(5): 8378-8389. doi: 10.1016/j.ceramint.2023.12.173
20. Fabriès J, Conquéré F, Arnaud G. The mafic silicates in the Saint Quay-Portrieux gabbro-diorite intrusion : crystallization conditions of a calc-alkaline pluton. Bulletin de Minéralogie. 1984; 107(6): 715-736. doi: 10.3406/bulmi.1984.7814
21. Xue B, Calvez L, Allix M, et al. Amorphization by mechanical milling for making IR transparent glass‐ceramics. Journal of the American Ceramic Society. 2016; 99(5): 1573-1578. doi: 10.1111/jace.14150
22. Qiu B, Wang F, Luo H, et al. Characterization and thermal behavior of granite waste during heating. Ceramics International. 2023; 49(11): 17052-17059. doi: 10.1016/j.ceramint.2023.02.066
23. Zhan J, Lu J, Wang D, et al. Scalable recycling of feldspar slime into high-quality concentrates by removal of colored minerals using the combined beneficiation processes. Separation and Purification Technology. 2023; 309: 123061. doi: 10.1016/j.seppur.2022.123061
24. Li C, Smith P, Bai X, et al. Effects of carbonate minerals and exogenous acids on carbon flux from the chemical weathering of granite and basalt. Global and Planetary Change. 2023; 221: 104053. doi: 10.1016/j.gloplacha.2023.104053
25. Yuguchi T, Hatsukawa H, Suzuki S, et al. Morphological and chemical characterization of secondary carbonates in the Toki granite, central Japan, and the evolution of fluid chemistry. American Mineralogist. 2022; 107(12): 2282-2290. doi: 10.2138/am-2022-8229
26. Greenwood JP, Hess PC. Congruent melting kinetics of albite: theory and experiment. Journal of Geophysical Research: Solid Earth. 1998; 103(B12): 29815-29828. doi: 10.1029/98jb02300
27. Lvov BV. Mechanism and kinetics of thermal decomposition of carbonates. Thermochimica Acta. 2002; 386(1): 1-16. doi: 10.1016/S0040-6031(01)00757-2
28. Zeng L, Sun H, Peng T, et al. The sintering kinetics and properties of sintered glass-ceramics from coal fly ash of different particle size. Results in Physics. 2019; 15: 102774. doi: 10.1016/j.rinp.2019.102774
29. Lu JS, Liu CY, Zhou J. Recycling of granite sludge for the preparation of high-strength glazed glass-ceramics using stepwise sintering. International Journal of Applied Ceramic Technology. 2024; 21(3): 1583-1592. doi: 10.1111/ijac.14727
30. Sánchez E, García-Ten J, Sanz V, et al. Porcelain tile: Almost 30 years of steady scientific-technological evolution. Ceramics International. 2010; 36(3): 831-845. doi: 10.1016/j.ceramint.2009.11.016
31. Geng X, Cao J, Wang Z, et al. Selective controlled precipitation mechanism of canasite and xonotlite in glass-ceramics from silica slag. Journal of Non-Crystalline Solids. 2020; 546: 120283. doi: 10.1016/j.jnoncrysol.2020.120283
32. Sen P, Pradhan BL, Lodhi L, et al. Precise measurement of Qn species distributions in modified silicate glass using phase-adjusted spinning sideband NMR experiment. Silicon. 2023; 15(18): 8065-8071. doi: 10.1007/s12633-023-02639-5
33. Tsomaia N, Brantley SL, Hamilton JP, et al. NMR evidence for formation of octahedral and tetrahedral Al and repolymerization of the Si network during dissolution of aluminosilicate glass and crystal. American Mineralogist. 2003; 88(1): 54-67. doi: 10.2138/am-2003-0107
34. Bao Z, Wang S, Miao L, et al. Preparation, properties and formation mechanism of transparent anorthite-based glass-ceramic glaze with high hardness. Ceramics International. 2024; 50(14): 26182-26192. doi: 10.1016/j.ceramint.2024.04.359
35. Jiang K, Xia M, Tang Y, et al. Formation of closed pore structure in CaO-MgO-Al_2O_3-SiO_2 (CMAS) porous glass-ceramics via Fe2O3 modified foaming for thermal insulation. Journal of the European Ceramic Society. 2023; 43(4): 1689-1697. doi: 10.1016/j.jeurceramsoc.2022.11.053

36. Colomban P, Kırmızı B, Simsek Franci G. Cobalt and associated impurities in blue (and green) glass, glaze and enamel: relationships between raw materials, processing, composition, phases and international trade. Minerals. 2021; 11(6): 633. doi: 10.3390/min11060633
37. Hrma P, Ferkl P, Kruger AA. Arrhenian to non-Arrhenian crossover in glass melt viscosity. Journal of Non-Crystalline Solids. 2023; 619: 122556. doi: 10.1016/j.jnoncrysol.2023.122556
38. Zhou J, Liu C, Lu J. Influence of $Ca(OH)_2$ modification on the pore structure and properties of porous glass-ceramics stepwise sintered from granite sludge. Construction and Building Materials. 2024; 429: 136436. doi: 10.1016/j.conbuildmat.2024.136436
39. Cheng X, Ke S, Wang Q, et al. Characterization of transparent glaze for single-crystalline anorthite porcelain. Ceramics International. 2012; 38(6): 4901-4908. doi: 10.1016/j.ceramint.2012.02.081
40. Huang H, Yu J, Liu F, et al. Preparation of a high-performance frit glaze using high-potassium feldspar. IOP Conference Series: Earth and Environmental Science. 2021; 943(1): 012018. doi: 10.1088/1755-1315/943/1/012018
41. Hasanuzzaman M, Islam F, Rashid A. Investigation of methods to prevent pin-holing defect in tableware ceramic industry. International Journal of Ceramic Engineering & Science. 2022; 4(6): 416-425. doi: 10.1002/ces2.10164
42. Zhong X, Cao L, Huang J, et al. Properties and evolutions of high-performance porcelain thin ceramic plates enhanced by multi-phase microstructure derived from sustainable smoky quartz tailings. Ceramics International. 2023; 49(2): 2540-2548. doi: 10.1016/j.ceramint.2022.09.233
43. Liu T, Deng C, Song J, et al. Preparation of self-foamed glass ceramics based on the cooperative treatment of various solid wastes: Characterization of structure-properties and analysis of self-foaming behavior. Ceramics International. 2023; 49(2): 2570-2582. doi: 10.1016/j.ceramint.2022.09.236
44. Amorós JL, Blasco E, Moreno A, et al. Effect of particle size distribution on the sinter-crystallisation kinetics of a SiO_2–Al_2O_3–CaO–MgO–SrO glass-ceramic glaze. Journal of Non-Crystalline Solids. 2020; 542: 120148. doi: 10.1016/j.jnoncrysol.2020.120148
45. Baila F, Labbilta T, Darmane Y. Feldspar purification from iron impurities: a review of treatment methods. Mineral Processing and Extractive Metallurgy Review. 2023; 45(6): 564-572. doi: 10.1080/08827508.2023.2217322